Chapter 5

Studies on photocatalytic degradation of MB with Lanthanum and Iodine co-doped TiO_2 nanoparticles

Abstract:

The photocatalytic degradation of methylene blue (MB) dye using Lanthanum (La) and Iodine (I) co-doped TiO_2 ($Ti_{1-x-y}La_xI_yO_2$, where x = 0.00 – 0.05, y = 0.00 – 0.005) nanoparticles prepared through the solution combustion method has been investigated in the current study. The photocatalysts' characterization was done using various techniques, including FTIR for identifying functional groups, XRD for determining crystallinity and crystallite size, DRS for estimating the band gap, and XPS for identifying elements and their oxidation states. The co-doping of La and I in TiO_2 causes narrowing the band gap and suppressing the recombination of e^-/h^+ pairs which surges its photocatalytic activity. The La and I co-doped TiO_2 nanoparticles exhibited a photodegradation efficiency of 98 % for MB within 40 min, significantly outperforming undoped TiO_2 and commercial TiO_2 photocatalyst Aeroxide P-25. Moreover, regeneration experiments demonstrated excellent reusability of the nanoparticles. To find potential use of photocatalytically treated water in irrigation, the phytotoxicity study was done with "*Vigna Radiata*" germination. The evaluation of phytotoxicity demonstrates that the treated water may be used for irrigation purposes.

5.1 Introduction:

This research describes the solution-combustion synthesis of La and I co-doped TiO_2 (LICT) photocatalysts with various molar ratios. This method creates fine TiO_2 particles by limiting their growth, which is easy and cheap. To aid in the preparation of nanoparticles, citric acid was utilised as fuel. Several techniques were used to characterise phase compositions, optical properties, and crystalline structure of the LICT. The

degradation of the MB dye in the UV Photochemical reactor served as the basis for investigating the photocatalytic performance of the photocatalysts. This dye was chosen because it is frequently found in textile effluent and exhibits excellent chemical and biological resistance to degradation by traditional processes. The influence of several variables, including pH, catalyst dose and initial dye concentration, were studied for their optimisation. The Table 5.1 mentions a brief of studies related to La-I co-doped TiO_2's use in degradation of various pollutants.

Table 5.1 Previous Literature related to La-I co-doped TiO_2

S.N.	Dopant Level	Pollutant	Intial conc.	Results	Ref.
1.	20% mole La, 20% mole I	Oxalic acid	Not mention	La-I-TiO_2 improved oxalic acid degradation, stabilizing anatase and inhibiting rutile transformation.	[1]
2.	2% mole La, 3% mole I	Reactive blue 19	50 ppm	98.6% degradation in 80 min under sunlight.	[2]

5.2 Materials and methods:

5.2.1 Chemicals Used:

The chemicals employed were Titanium (IV) dioxide (TiO_2, 99% pure), ammonium sulphate GR [$(NH_4)_2SO_4$], sulfuric acid (H_2SO_4) 98% concentrated, liquid ammonia of 25% concentration (sp. gr. is 0.91), lanthanum nitrate [$La(NO_3)_3.6H_2O$] of purity 99%, Iodic acid (HIO_3), citric acid monohydrate GR ($C_6H_8O_7H_2O$), Nitric acid GR (HNO_3) and MB dye. The materials mentioned above were bought from Merck, India.

5.2.2 Preparation of undoped TiO_2 and LICT nanoparticles:

Primarily, TiO_2 powder was used to prepare undoped TiO_2 and LICT ($Ti_{1-x-y}La_xI_yO_2$) by the solution-combustion technique. The molar ratio of ammonium sulphate to titanium (IV) dioxide in the solvent (100 ml of H_2SO_4) was 1:6. The resultant solution was heated for 2-3 h at 170 °C and 400 rpm while being stirred, continuing to synthesise titanium oxysulfate [$TiO(SO_4)$]. In separate beakers, the calculated amounts of lanthanum nitrate and iodic acid were added to 100 mL of sulfuric acid, and this was heated for 2 h at 170 °C and 400 rpm. The weight of various materials is given in Table 5.2 for different mole ratios of La, and I, and catalyst coding is also mentioned in the Table 5.2 which has been used throughout this paper. Once the mixture had cooled to room temperature, 25 % ammonia solution (NH_3) was added very slowly until a white precipitate formed. This precipitate was collected and dissolved in 70 % nitric acid. In this, 10 g of citric acid monohydrate was added, and the volume was made up to 500 mL with distilled water. The solution was evaporated at 80^oC; self-ignition started in an open atmosphere at ambient temperature, resulting in the emission of numerous gases and forming a fluffy brown LICT mass that was subsequently ground into a fine powder using a mortar and pestle. Citric acid serves as a complexing agent by forming a complex with cations, and providing fuel for the combustion process during ignition. The ignition stage raised the temperature, making crystalline powder possible to form at a low temperature. This powder was calcined at 500°C for 5 h. to get final LICT nanoparticles.

Table 5.2 The weight of various materials for different mole ratios of La, and I co-doping with catalyst coding.

Mole % Doping			**Weight Required(g)**		
Catalyst Code	La	I	$La(NO_3)_3.6H_2O$	HIO_3	TiO_2
T0	0	0	0.000	0.000	5.012
T1	1	1	0.271	0.110	4.618
T2	1	2	0.271	0.220	4.508
T3	1	3	0.271	0.330	4.398
T4	1	4	0.271	0.440	4.288
T5	1	5	0.271	0.551	4.178
T6	2	1	0.542	0.110	4.348
T7	2	2	0.542	0.220	4.238
T8	2	3	0.542	0.330	4.128
T9	2	4	0.542	0.440	4.017
T10	2	5	0.542	0.551	3.907
T11	3	1	0.813	0.110	4.077
T12	3	2	0.813	0.220	3.967
T13	3	3	0.813	0.330	3.856
T14	3	4	0.813	0.440	3.746
T15	3	5	0.813	0.551	3.636
T16	4	1	1.084	0.110	3.806
T17	4	2	1.084	0.220	3.696
T18	4	3	1.084	0.330	3.585
T19	4	4	1.084	0.440	3.475
T20	4	5	1.084	0.551	3.365
T21	5	1	1.355	0.110	3.535
T22	5	2	1.355	0.220	3.424
T23	5	3	1.355	0.330	3.314
T24	5	4	1.355	0.440	3.204
T25	5	5	1.355	0.551	3.094

5.2.3 Characterisations:

XRD analysis was used to identify the phases of the prepared LICT photocatalysts and the average crystallite size using Cu K irradiation (Ultima IV; Rigaku, Japan). XPS analysis (AMICUS, Kratos Analytical, UK) was used to estimate the binding energy (BE)

of the elements in the samples using a monochromated Mg K (1253.6 eV) X-ray source. With barium sulphate used as an internal reference, the UV-Vis absorption spectra of the prepared LICT photocatalysts were examined by DRS (CORY 100 Bio UV spectrophotometer). The Kubelka-Munk technique was used to determine the indirect band-gap energy (Eg) of the LICT photocatalysts by plotting $[F(R)\times h]^{1/2}$ vs the photon energy ($h\nu$). The IR spectra were recorded using the KBr pellet method with the Nicholet 5700 (Thermo Electron) FTIR spectrophotometer. The photocatalytic activity was evaluated for all prepared and regenerated photocatalysts by recording concentration reduction with time, i.e., by knowing the kinetics of photocatalytic reaction.

5.2.4 Procedure of kinetic study:

The degradation kinetics was investigated using a quartz tube in the photochemical reactor with all prepared catalysts. Five different aqueous dye solution concentrations were used in the experiments (10, 20, 30, 40 and 50 ppm). This quartz tube contained 100 mL of dye solution and LICT photocatalysts. The stirrer and UV lamp were turned on. 2 mL samples were taken out at 5 min intervals for 1 h, and their dye concentration was assessed after the centrifugation of samples.

The photocatalytic performance of regenerated LICT nanoparticles was evaluated, a similar experimental approach as described previously. Only regeneration of the T8 photocatalyst was explored in this work since it has demonstrated the highest photocatalytic performance of all the prepared photocatalysts.

Based on the kinetic tests, the photocatalytic performance of bare and regenerated T8 photocatalyst was investigated in the photochemical reactor at dye concentrations of 30 ppm through degradation kinetics. A photocatalytic degradation of 30 ppm dye solution under the same experimental circumstances was used to compare the prepared undoped TiO_2, the best catalyst T8, and Aeroxide P-25 (Sigma Aldrich).

5.3 Results and discussions:

The results of different characterization of photocatalysts and other experiments are as follows:

5.3.1 Characterizations of photocatalysts:

5.3.1.1 XRD:

Figure 5.1 (a) shows XRD patterns of both undoped and LICT nanoparticles. The peaks at 2θ = 25.27, 37.76, 48.04, 53.89, 55.07, 62.61 and 75.10 correspond to (101), (112), (200), (105), (211), (204), and (215) planes demonstrate that the samples contain anatase phase and crystalline structure of TiO_2 (JCPDS 21-1272) [3].

In the XRD patterns of LICT nanoparticles, only the diffraction peaks of the anatase phase are evident. These findings suggest that co-doping with La and I stabilized the anatase phase by inhibiting the transition to the rutile phase [2]. The photocatalytic activity of TiO_2 in the anatase phase is much greater than that of TiO_2 in the rutile phase. Since anatase traps holes at a rate 10 times higher than rutile, it also has a low recombination rate [4]. Doping with La might prevent the transition from the anatase to rutile phase. The formation of La_2O_3 occurs predominantly at the grain boundaries. This segregation acts as a physical barrier that impedes the growth of TiO_2 crystals, effectively stabilizing the anatase phase by preventing its transformation into the denser rutile phase. This stabilization is crucial for maintaining high photocatalytic activity as anatase is more active than rutile. Additionally, La_2O_3 at the grain boundaries restricts crystal growth, resulting in smaller crystallite sizes which enhance photocatalytic activity due to increased surface area and more active sites [5, 6].

The ionic radius of Lanthanum is 1.03 Å, which is greater than that of Titanium 0.62 Å; therefore, La was unable to replace the Ti ion, and the leftovers that were found in the interstitials of Titanium dioxide that were located under the range of scan for XRD. Since

the radius of La ions is more than that of Ti ion, lanthanum oxide (La_2O_3) linkage may form at the anatase surface instead of La^{3+} being assimilated into the TiO_2 lattice. The La_2O_3 peak in the XRD pattern could not be located because it is distributed [6] and also no iodine peak was found that suggests that the I^{5+} ions are effectively incorporated into the TiO_2 lattice [7].

However, after being co-doped with La and I ions, the phase change from amorphous to anatase TiO_2 is drastically suppressed, as evidenced by a decrease in the relative intensity of the diffraction peak pertaining to the (101) face of anatase TiO_2 phase. Further, the crystallite size of LICT decreases when doping of La is increased up to 2% and doping of I is increased up to 3%, indicating that La can impede the growth of crystallite size due to the segregation of dopant cations at the grain boundary [8] and I doping inhibit the phase transformation from anatase to rutile phase. This inhibition of the phase transformation may be due to the formation of Ti-O-I bonds, and the doped I^{5+} ions may act as a ligand for the Ti(OH)n ions. Furthermore, this phenomenon reduces the crystallite size of TiO_2, which in turn slows down the formation of the rutile phase [9]. Co-doping with iodine introduces further lattice distortions and defect sites, such as oxygen vacancies, improving electron-hole separation and extending light absorption into the visible spectrum. These modifications collectively enhance the photocatalytic efficiency of TiO_2, making it more effective for applications like pollutant degradation under solar irradiation [10,11].

Figure 5.1 (b) shows the shift of diffraction peak ($2\theta = 25.27$) to the lower theta values as a consequence of the larger radius of both La^{+3} (1.03 Å) and I^{5+} (1.09 Å) [12], compared to that of Ti^{4+} (0.61 Å) by the Bragg equation: $2d\sin\theta = \lambda$. The average crystallite size of T0 and T8 calculated by equation 2.3 was 36.18 and 13.76 nm, respectively.

A minor broadening of the full width at half maximum intensity (FWHM) of the peaks

for the LICT nanoparticles occurred, which indicated a reduction in the crystallite size [13].

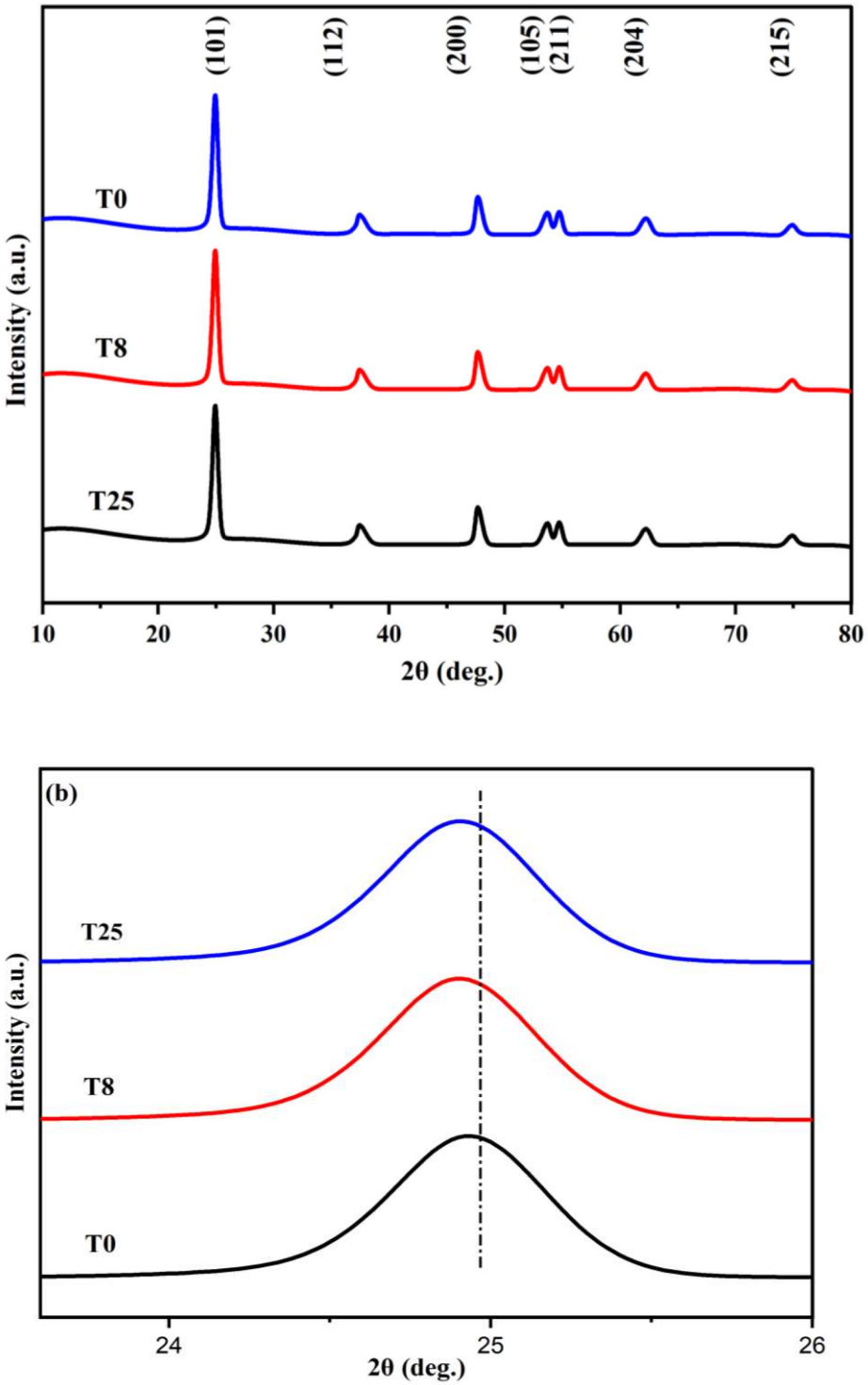

Figure 5.1 XRD diagram of (a) selective LICT and undoped TiO_2 photocatalysts, (b) enlarged view of (101) peak.

5.3.1.2 FTIR:

Figure 5.2 illustrates the FTIR spectra of prepared photocatalysts. The broad band at 1002 cm^{-1} is because of the vibrational modes of Ti-O [14]. The widening absorption peaks at 1622 cm^{-1} and 3420 cm^{-1} are attributed to bending and stretching vibrations of hydroxyl functional groups linked to the surface. The presence of hydroxyl bonds on the surfaces of samples enhances their catalytic efficiency due to their beneficial effects on the production of highly reactive hydroxyl radicals during the reaction process [15]. The values observed by Akbar et al. [16] are also in a comparable range with our results. There is also evidence that I-doping strengthens the hydroxyl stretching and bending vibrations of absorption peaks and that the peaks get stronger as the I-doping concentration rises. Increased hydroxyl stretching and bending vibrations in FTIR spectra indicate a higher density of surface hydroxyl groups on iodine and lanthanum co-doped TiO_2 nanoparticles. These groups are crucial for generating hydroxyl radicals under UV light, enhancing photocatalytic degradation of pollutants. This is attributed with the fact that when iodine is doped in TiO_2, various species, such as $IO_4^-/IO_3^-/I^-$ are formed and have played an essential part in improving the photocatalytic performance of catalysts in degradation of MB dye [6].

The broader peaks at 3151 cm^{-1} correspond to H-I-H stretching, and the strength of the absorption peak increased with increase in I-doping concentration [11]. Barkul et al. [17] observed comparable H-I-H stretching and bending vibration ranges. La doping moves the distinctive peak to 480 cm^{-1}, which may correlate to the bond of Ti-O-La. Bare TiO_2 (without La or I doping) exhibits a band at 512 cm^{-1}, a typical peak of TiO_2. Sibu et al.[18] likewise showed comparable ranges for their results. Consequently, it is evident from the above explanation that the FTIR plot, Figure 5.2 validates the doping of La and I. This shifts and broadening in specific FTIR peaks, such as the 3151 cm^{-1} H-I-H stretching and

480 cm^{-1} Ti-O-La bond, suggest iodine-induced modifications in hydrogen bonding and La-induced lattice distortions, respectively. These changes modify the electronic structure, reduce the band gap, and allow greater visible light absorption, significantly improving photocatalytic activity. Iodine and lanthanum also create defect sites that enhance charge separation and reduce recombination rates, boosting the efficiency of photocatalytic reactions [19,20].

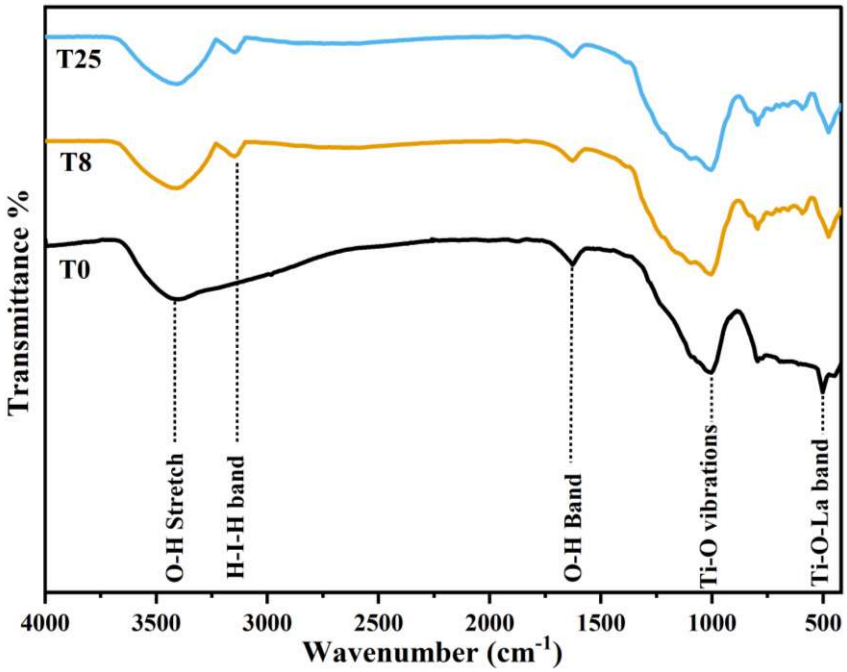

Figure 5.2 FTIR plots of selective LICT and undoped TiO_2 photocatalysts

5.3.1.3 DRS:

The UV-Visible range was used to determine the optical response of the synthesised LICT and bare TiO_2, which are illustrated in Figure 5.3. In present study indirect band-gap of bare and LICT nanoparticles was determined by $[F(R\alpha)\times h\upsilon]^{1/2}$ vs hυ plot. Here F(Rα) can be represented by the Kubelka-Munk relation and given as follows:

$$F(R\alpha) = \frac{(1-R\alpha)^2}{2\times R\alpha} \qquad (5.1)$$

Where $R\alpha = 10^{-A}$ is the reflectance coefficient which can be calculated from absorbance data.

The results indicate that adding metals to TiO_2 photocatalysts leads to a slight decrease in band-gap. This change might be attributable to the dielectric confinement effect. Since O_2 has a 2p orbital, charge moves from the valence band to the conduction band of TiO_2, and the dielectric constant of La_2O_3 is smaller than that of TiO_2, the energy change caused by dielectric confinement (which happens when La is added) is bigger than the energy change caused by space limits on electron holes. The observed displacement of spectral lines towards longer wavelengths is called Red-shift [21]. The reduction of bandwidth by the interaction of I 5p with Ti 3d states and the transition of O 2p states to higher energy in Ti^{4+} ions cause the shifting of the absorption band due to I-doping. The presence of iodine in the TiO_2 lattice, which causes crystallographic defects in TiO_2 is an additional cause of the absorption band shifting [9]. Bagwasi et al. identified comparable causes (bandwidth narrowing and doping-induced crystal defect) for the absorption band shift [22]. This band shift implies that I^{5+} and La^{3+} were successfully doped into TiO_2 [9,23]. It is clear from Figure 5.3 the Eg for undoped TiO_2 is 3.2 eV and for T8 sample is 2.68 eV. The photocatalytic efficiency of La and I co-doped TiO_2 nanoparticles is enhanced due to the red shift in UV-visible absorption spectra and decreased band-gap energy. The red shift, resulting from iodine-induced mid-gap states and La-induced lattice distortions, enables absorption of visible light by introducing additional energy levels and modifying the electronic environment [9, 24-25]. This effect, coupled with dielectric confinement, improves light absorption and charge carrier localization. Decreased band-gap energy, facilitated by iodine and lanthanum doping creating defect states and lattice distortions, allows for lower-energy light absorption. This synergy boosts photocatalytic activity by enhancing light absorption, extending charge carrier lifetime, and increasing surface

reactivity [21,26]. Lanthanum at grain boundaries further stabilizes the anatase phase, maintaining high photocatalytic efficiency [6].

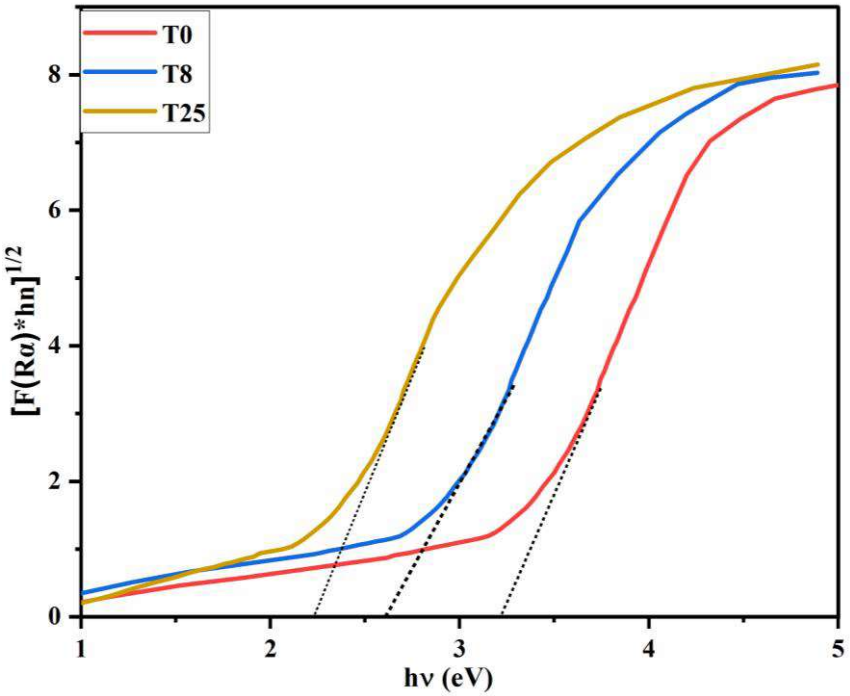

Figure 5.3 DRS plots of selective LICT and undoped TiO_2 photocatalysts

5.3.1.4 XPS:

XPS analysis was performed on LICT and undoped samples to determine the presence of elements and their oxidation states. The respective elements were present in the samples. Figure 5.4 (a) depicts the XPS spectra of the 2p orbital of Ti in bare and LICT. Both co-doped and undoped samples exhibit two distinct peaks attributable to Ti $2p_{3/2}$ and Ti $2p_{1/2}$, showing that Ti^{4+} is the predominant oxidation state of titanium in anatase TiO_2 [27]. The undoped sample of TiO_2 exhibits binding energy (BE) values of 458.9 eV and 464.6 eV [28]. Due to co-doping, these peaks move toward higher BE, i.e., greater than 0.2 eV, indicating several electronic interactions between Ti and La oxides. The variation in

electronegativity results in reduction of the external electron density of titanium, causes increment in the BE of Ti 2p [29]. Figure 5.4 (b) depicts the XPS pattern for O 1s. The bare TiO_2 sample exhibits at BEs of 529.28 and 531.08 eV, which belong to the lattice O_2 and OH group, respectively. The T8 sample exhibits three distinct peaks, with two of them are similar as in undoped one but with a rise of more than 0.2 eV. Furthermore, the third one is detected at a BE of 532.43 eV, corresponding to the La-O bond, as supported by FTIR. Figure 5.4 (c) depicts La 3d spectra of LICT. The diagram displays peaks indicative of the spin-split orbit levels La $3d_{3/2}$ and La $3d_{5/2}$. These peaks demonstrate the existence of La^{3+} entities at 855.3 and 837.1 eV, respectively [30,31]. According to the literature, the reported BEs for the 3d shifting of Lanthanum are 852 and 835 eV. However, it has been discovered that these peaks undergo an upward shift to higher energy values. This shift is ascribed to the substitution of Ti^{4+} with La^{3+}. It is apparent that La does not integrate into TiO_2 lattice but rather exists within in the form of Ti-O-La bond [32-34]. La is less electronegative than Ti, which causes a charge imbalance in doped TiO_2. Consequently, this change in the BE of La decreases Ti-O-La electron density [35].

In Figure 5.4 (d), the XPS spectrum of I 3d is depicted. The presence of peaks at 623.1 and 618.8 eV, corresponding to I $3d_{3/2}$ and I $3d_{5/2}$, indicates the presence of I^{5+} and I^- ions. The charge imbalance resulting from the substitution of Ti^{4+} with I^{5+} causes the formation of I^-. The capability of I^{5+} to form a transitional energy level below the conduction band of TiO_2 leads to a reduction in the Eg and an increase in the lifetime of electron-hole pairs [36]. I^{5+}/I^- pairs were detected in I-doped TiO_2, and I^{5+} ions replaced Ti^{4+} in the Ti–O–I link, as demonstrated by the results [37]. The presence of both iodine ions in the synthesised photocatalyst, as reported by Saroj et al., indicates the creation of Ti-O-I link via replacement of I^{5+} for Ti^{4+} ions. Since both ions operate as electron acceptors, the presence of these ions ensures the splitting of photogenerated pairs of electron and hole

and limits their recombination [9].

As it is earlier discussed in Figure 5.4 (a) compared to un-doped TiO_2 nanoparticles, the Ti 2p peak of LICT nanoparticles moved slightly towards higher BE. This could be explained by the fact that iodine has higher electron negativity, and La has smaller electron negativity than titanium. Because of this, adding La and I to the TiO_2 structure a change in the electron density occurred in the vicinity of the Ti cations. This affirmed the La and I were co-doped successfully to the TiO_2 crystal [38].

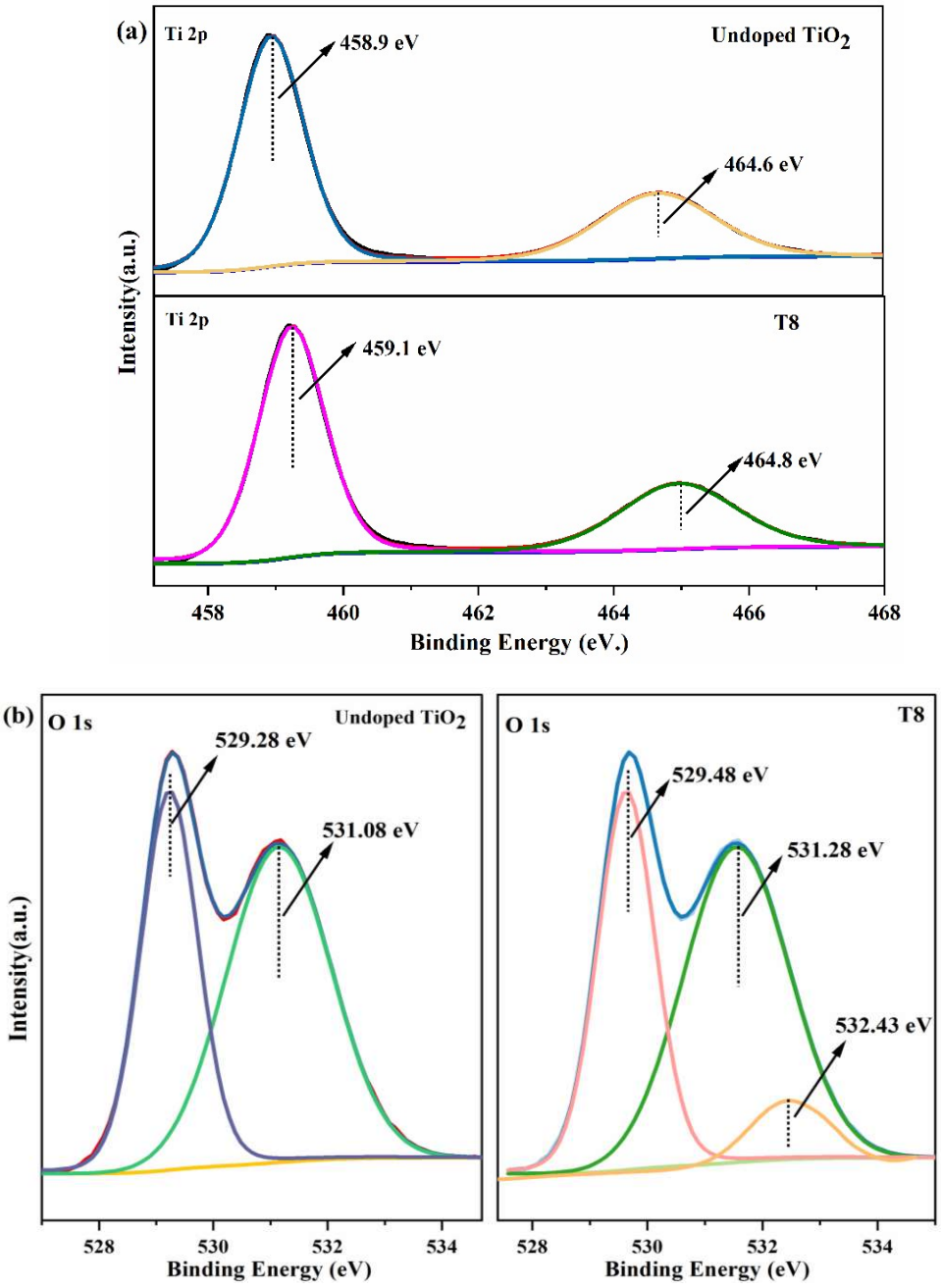

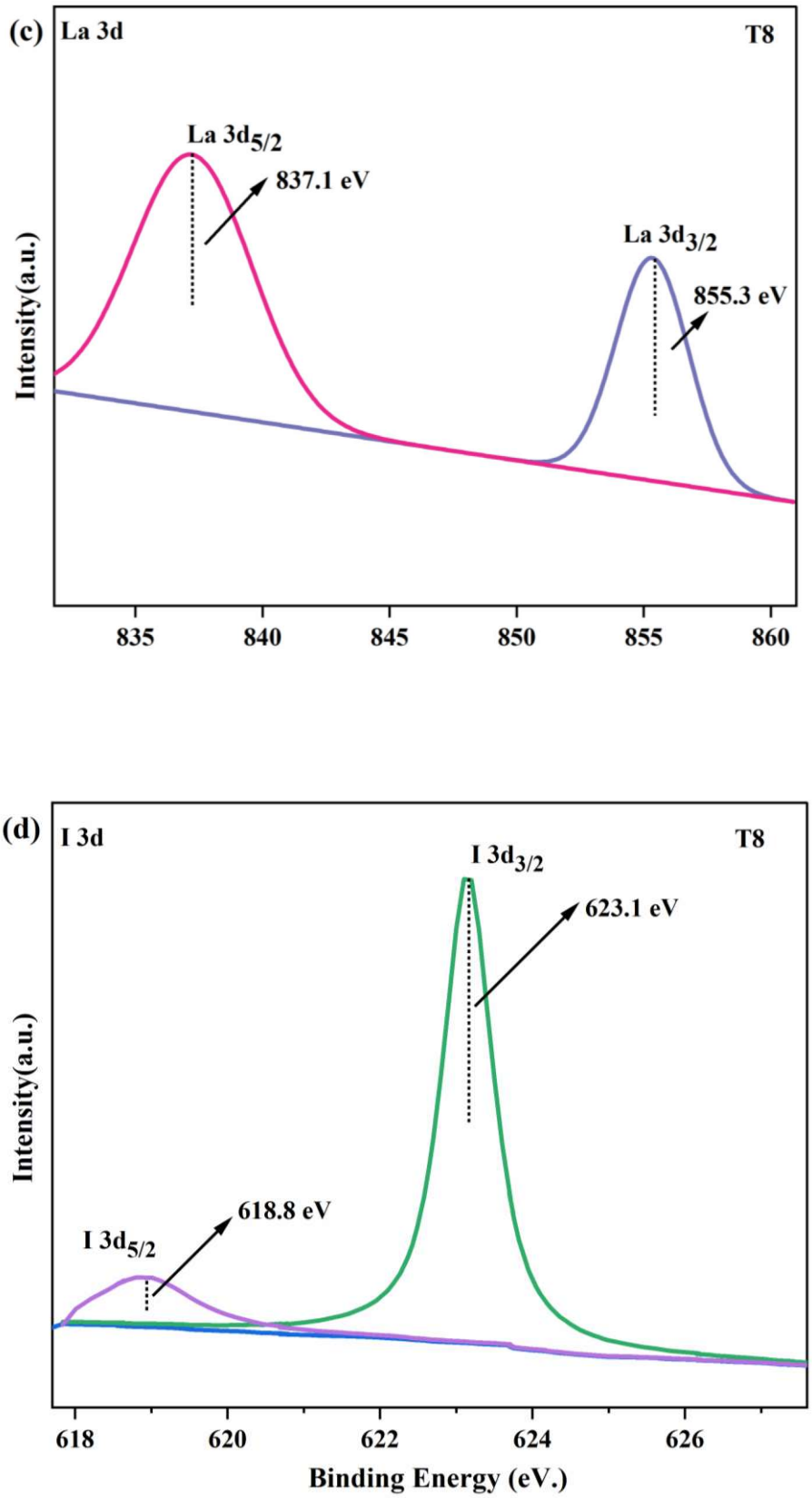

Figure 5.4 XPS spectra of (a) fitting curves of the Ti 2p regions (b) fitting curve of O 1 s region of undoped and T8 (c) fitting curves of La 3d regions (d) fitting curve of I 3d region

5.3.1.5 HR-TEM:

The morphology and the crystallite size of the synthesized photocatalysts were determined using HR-TEM analysis.

From Figure 5.5 (a), the HR-TEM image of the T8 photocatalyst is found to be spherical, and these nanoparticles seem to be overlapped with each other and also agglomerated due to the high surface energy [31,39]. The selected area electron diffraction (SAED) in the inset of Figure 5.5 (a) shows that the particle's anatase phase is visible based on the anatase (101) main peak, which is also confirmed by XRD analysis. SAED images also indicated the highly crystalline structure of the T8 photocatalyst [15,40].

With the help of histogram data, shown in Figure 5.5 (b), the average particle size of the T8 photocatalyst was calculated. The synthesized T8 photocatalyst has an average particle size of 17.46±4.03 nm. The average particle size obtained from HR-TEM analysis has good agreement with the average particle size that was calculated using Scherrer's formula in the XRD analysis, as observed in the particle size histogram.

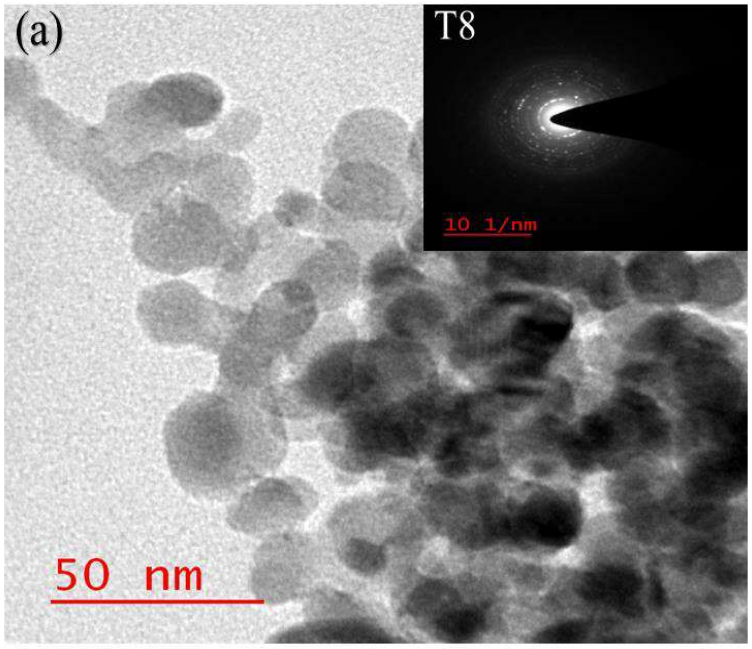

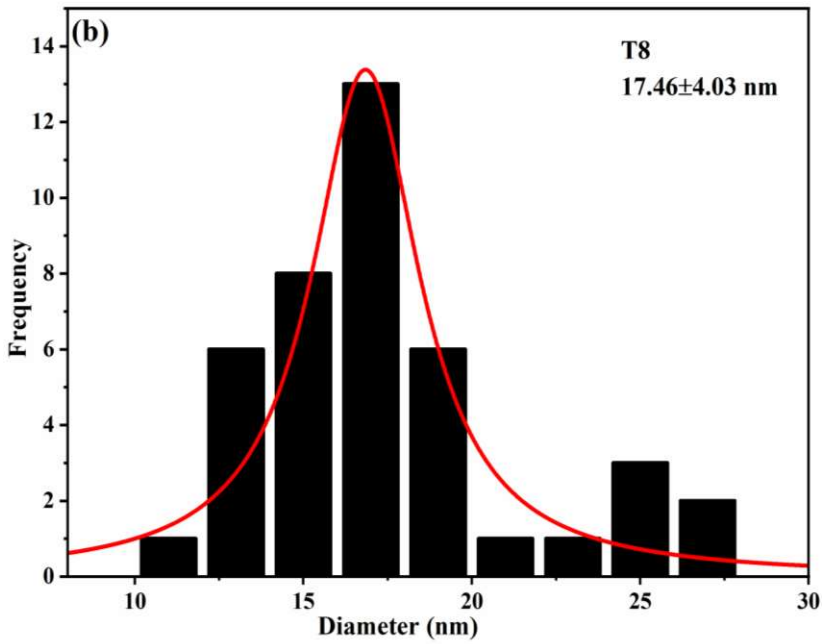

Figure 5.5 HR-TEM and SAED image of T8 photocatalyst (b) and Particle size distribution of T8 photocatalyst

5.3.2 Photodegradation of MB dye:

Photodegradation of MB dye in aqueous solutions of different dye concentrations (10, 20, 30, 40 and 50 ppm) with all catalysts was performed, and results are given in Table 5.4. The procedure for the photodegradation of MB dye is already discussed in section 2.5. It is clear from Table 5.4 that photocatalyst T8 has the highest value of the rate constant at each dye concentration. So, for further analysis, only the T8 catalyst is considered.

The potential of LICT and bare TiO_2 photocatalysts to degrade MB dye in UV light was tested by running different experiments with different reaction parameters. Before standardising the reaction conditions, test runs were done to determine how variables like UV light and catalyst affected each other.

Only the MB dye (without photocatalysts) trial degradation tests were done for 1 h, both with and without light. In both cases, the results show that UV light does not affect how MB dye degrades.

A quartz tube was loaded with 100 mL of dye solution and 0.01 g of catalyst, and the mixture was agitated for 60 min in the dark. After that, the absorbance was measured at the λ_{max}. The dye solution at equilibrium had a slight reduction in its absorbance and hence in concentration reason being dye adsorption on the catalyst, which was about 2%.

It is desirable for propagation of photocatalytic reaction. In the final step, the dye solution and the catalyst were placed inside a quartz tube and agitated for an hour under ultraviolet light. The absorbance was then measured. The absorbance decrease shows that UV light was responsible for activating the catalyst and producing hydroxyl radicals, which degrade the dye molecules [41].

The effects of different parameters pH, initial dye concentrations, and catalyst amounts were studied to find the best values of these parameters with time. Throughout this investigation into the consequences of these reaction characteristics, one of the parameters was altered while the others remained the same.

5.3.2.1 Effect of pH:

The effect of different pH (3, 4, 5, 6, 7, 8, 9 and 10), a significant parameter, on the photodegradation of MB is illustrated in Figure 5.6. This shows that photocatalytic activity is highest at 9 pH. Since in photocatalytic reaction strong oxidants $OH^{\cdot}$ radicals are generated, responsible for MB's photocatalytic degradation [42]. So, low pH is not advantageous because combining hydroxyl groups with several protons prevents the formation of $OH^{\cdot}$, which significantly decreases the dye degrading efficiency. However, when the pH is significantly high, the surface of the TiO_2 becomes negatively charged. This causes hydroxyl ions to build up. Because of this, the surface of the TiO_2 becomes less active, and the rate of degradation slows down [43].

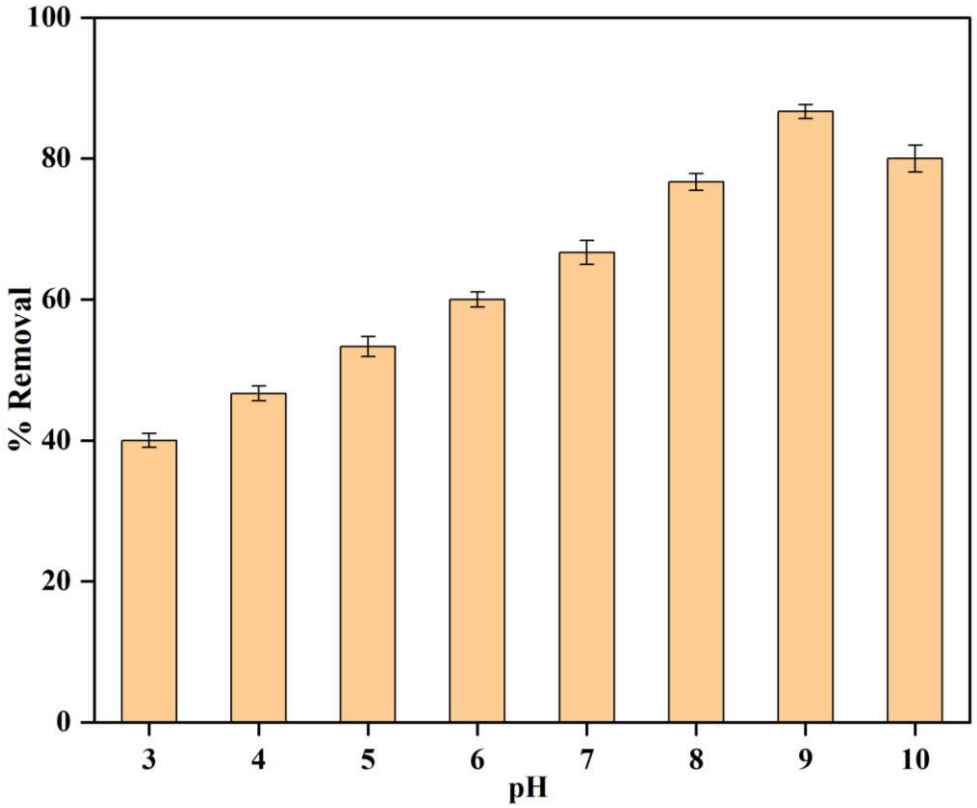

Figure 5.6 Effect of pH on removal of MB dye by T8 photocatalyst at initial concentration of 30 ppm and catalyst dose of 0.1 g L^{-1}

5.3.2.2 Effect of photocatalyst loading:

Fixing the right amount of catalyst to be used during the photocatalytic reaction is a better way to get more photons and avoid wasting the catalyst. In this case, to find the best amount of catalyst was found by conducting experiments with different loading from 0.02 to 0.14 g L^{-1} while other conditions remained the same. Degradation studies were carried out at pH 9 and 30 ppm MB concentration. With increased catalyst loading (0.02 to 0.1 g L^{-1}), an increase in degrading efficiency was observed. The maximum removal efficiency (93.33%) was found at 0.1 g L^{-1} [44].

Whereas further increase in catalyst loading (0.1 to 0.14 g L^{-1}) the degrading efficiency decreased. Krishnan and Shriwastav [44] have suggested increasing the loading upto the optimum value; the overall number of active sites on the catalyst surface increases with

an increase in catalyst loading, produce more OH• radicals which contribute to dye degradation. The decrease in activity beyond optimal value may be because of resistant to the light approach to nanoparticles' surface. Moreover, aggregated particles may occur due to excessive photocatalyst use [43]. The best loading for photodegradation of MB was 0.1 g L^{-1} as evidenced by Figure 5.7.

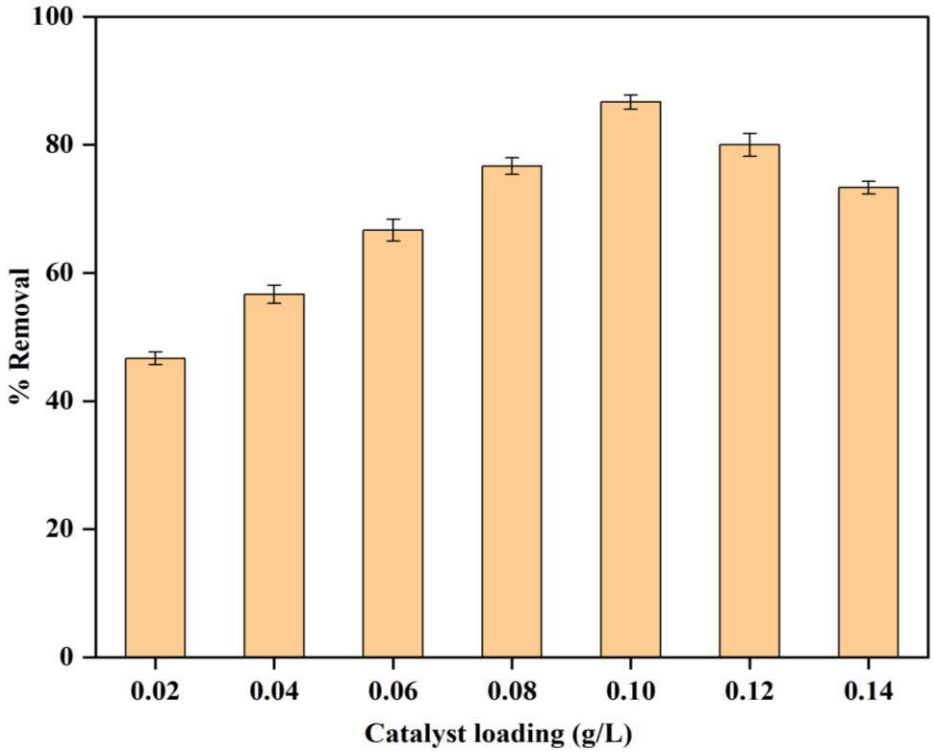

Figure 5.7 Effect of catalyst loading on the removal of MB dye by T8 photocatalyst at initial concentration of dye 30 ppm and pH 9

5.3.2.3 Effect of initial dye concentration:

Furthermore, at pH 9, using 10, 20, 30, 40, and 50 ppm of initial dye solution for T8 catalyst, how the starting concentration of MB affects the rate of photocatalytic degradation was studied. Figure 5.8 displays the experimental results, which show that the concentration of the dye significantly affects the degradation rate. Degradation rates in 40 min for 10 ppm, 20 ppm, 30 ppm, 40 ppm and 50 ppm are 98%, 95%, 93.33%, 90% and 88%, respectively. The explanation for difference in degradation rate is that the concentration of dye molecules rises, the quantity of available sites on the photocatalyst's surface remains constant, meaning fewer molecules can be degraded at any given time. In addition, a higher dye concentration causes a large number of molecules available for adsorption on the catalyst, limiting the amount of light that may reach the catalyst's active sites. So, fewer OH· are formed, resulting in low MB dye degradation [21].

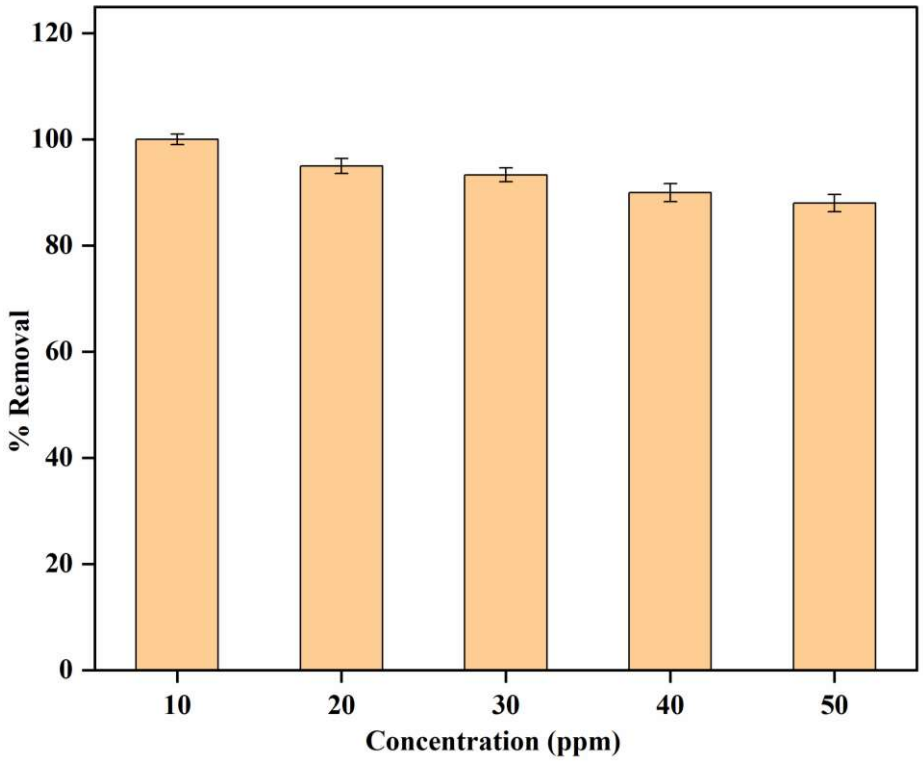

Figure 5.8 Effect of concentration on the removal of MB dye by T8 photocatalyst at a catalyst dose of 0.1 g $L^{-1}$and pH 9

Table 5.3 Comparison of photocatalytic activity (MB degradation) of various doped TiO_2 Photocatalysts

Catalyst	Optim. doping	Poll.	Reactor (Light source)	Time (min)	Rate Constant (min^{-1})	% Deg.	Ref.
Na doped TiO_2	8% mole	MB	300 W high-pressure ultra vitalux lamp	60	0.043	92.5	[45]
Sn doped TiO_2	5% mole	MB	125 W Hg lamp (UV), Visible light	120	0.1629 (UV), 0.0123(Visible)	98 (UV) 77 (Vis.)	[46]
Bi-doped TiO_2	10% mole	MB	32 W fluorescent lamp	150	0.006	64	[47]
Fe-N co-doped TiO_2	1% Fe & % N	MB	25 W fluorescent lamp	300	Not Reported	80.5	[48]
S-Ni co-doped TiO_2	1.02% Ni & 1.12% S wt	MB	500 W halogen lamp	180	Not Reported	85	[49]
Bi-doped TiO_2	1% wt	MB	250 W Hg lamp	120	0.0012	80	[50]
Ni-Cr co-doped TiO_2	6% Ni& 4% Cr wt	MB	Sunlight	90	0.0366	95.6	[51]
La- I co-doped TiO_2	2% La & 3% I	MB	UV Photo-chemical Reactor with 8W of 8 tubes	40	0.060	98	Present Work

5.3.2.4 Overall optimum conditions for Degradation of MB dye

Performance of T8 catalyst was the best at catalyst loading of 0.1 g L^{-1}, pH of 9, and an initial dye concentration of 10 ppm. The performance of different material doped TiO_2 catalysts for degradation of MB dye reported in the literature is given in Table 5.3. It is inferred that a semiconductor material could photocatalyse the pollutants in an effective way. Compared to the catalysts reported in literature, our T8 catalyst works better in UV light.

5.3.3 Scavenger Studies on LICT photocatalysts for MB dye degradation:

The present study aimed to explore the impact of scavengers, namely isopropanol (OH^- scavenger), EDTA (h^+ scavenger) and ascorbic acid (O_2^- scavenger) at overall optimum conditions for degradation of MB dye was investigated. The % degradation for MB dye was 98% for T8 photocatalyst without addition of any scavenger. The results indicated that the degradation rate decreased from 98% to 58.67%, 74.35%, and 83.65% when isopropanol, EDTA, and ascorbic acid were added to the system, respectively. These results are also consistent with previous scavenger studies on doped TiO_2 photocatalysts for the degradation of dyes [52-54].

So, the primary reactive species involved in the photocatalytic degradation of MB dye is hydroxyl radical (•OH). Furthermore, significant inhibition of MB dye degradation was also observed in the presence of EDTA, indicating the substantial involvement of h^+ in the photocatalytic process [57].

The addition of scavengers resulted in the reduction of degradation in all cases, indicating the participation of various species, namely $OH^•$, h^+ and O_2^{-}, in the photocatalytic degradation process. As described in the mechanism, these species played a crucial role in the degradation process [54].

5.3.4 Possible Mechanism:

In order to act as electron trap sites near nanocrystalline TiO_2, La-doping produces oxygen vacancies, which provide shallow energy states at the bottom of the conduction band. The shallow energy states introduced by rare earth ion (La) in the top valence band, function as hole trap sites. Such trapping is attributable to the separation of the charge carriers. Charge carriers then move to the photocatalyst's surface to begin redox processes, enhancing the photocatalytic activity of the photocatalyst [56]. Lan et al. [33] suggest that doping of La may alter Ti^{4+} to Ti^{3+} by charge compensation. La doping may result in the

formation of impurity levels due to interactions between Ti^{3+} and oxygen vacancies, which might limit the recombination of charge carriers. Also, La_2O_3 may transmit electrons to the TiO_2 surface, which is beneficial for photocatalytic activity [57]. In addition, the light penetration depth into titania much exceeds that of space charge film when the dopant concentration is very high. Space charge area becomes extremely limited; consequently, the recombination of the electron-hole pairs generated by the photoexcitation process becomes more straightforward [32].

The iodine doped TiO_2 yields $IO_4^{\cdot}/IO_3^{\cdot}/I^-$ species, which play an essential role in the improvement of the photocatalytic activity of TiO_2 because IO_4^- and IO_3^- intermediates create highly reactive IO_3 and IO_4 free radicals. These free radicals are accountable for the oxidation of MB. The existence of additional iodine states I^{5+} (verified by XPS analysis) suggests improved electron-hole separation, which inhibits the recombination as I^{5+} functions as an electron acceptor. The created holes can immediately react with hydroxyl groups (adsorbed on the surface), generating OH free radicals that play a crucial role in photocatalytic dye degradation [9]. From the preceding explanation, it is evident that the synergistic impact of La and I co-doped TiO_2 improves the photocatalytic degradation of MB dye.

The following describes the process by which LICT efficiently absorbs protons from UV light:

$$LICT + h\nu \rightarrow h^+_{vb} + e_{cb}^- \quad (5.2)$$

The production of hydroxyl and superoxide radicals because of the neutralisation by photo holes and electrons, respectively, is demonstrated by the following:

$$LICT(h^+) + H_2O/OH^- \rightarrow LICT + H^+ + \cdot OH \quad (5.3)$$

$$LICT(e^-) + O_2 \rightarrow LICT + O_2^{\cdot -} \quad (5.4)$$

Oxidation of MB by consecutive attacks of OH and O_2 radicals:

$OH\cdot + MB \rightarrow$ Simpler products (5.5)

$O_2^{\cdot -} + MB \rightarrow$ Simpler products (5.6)

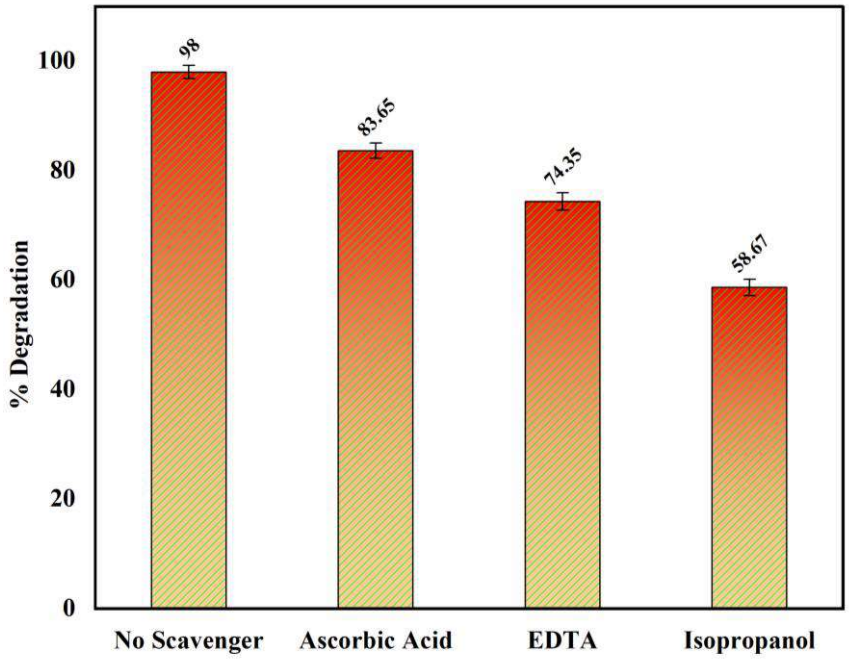

Figure 5.9 Effect of different Scavengers on Photocatalytic degradation of MB dye.

5.3.5 Kinetics study of degradation of the dye with LICT photocatalysts:

All catalysts were subjected to kinetic studies, of which Figure 5.10 and Figure 5.11 depict kinetic data for MB dye degradation with T8 photocatalyst. The presented figures display the concentration vs time and -ln(C/Co) vs time plots. The obtained high R^2 values indicate that the degradation kinetics of MB with all the catalysts can be adequately described by pseudo-first-order kinetics Eq. (5.7).

$$-dC/dt = k_pC \quad (5.7)$$

Based on the -ln(C/Co) vs time graph, the k_p values were calculated and presented in Table 5.4, with their corresponding R^2 values. It is observed from this table that the rate constant exhibited a linear increase as the doping of La was increased up to 2 % in

conjunction with a simultaneous increase in, I doping up to 3 %. However, beyond these doping concentrations, the rate constant decreased. This decrease can be attributed to light scattering phenomena, leading to an increase in the optical density of the suspension at the wavelength of the incident light. The increase in doping levels of La and I initially enhanced the photocatalytic activity, leading to a higher rate constant. This can be attributed to the enhanced charge carrier separation and the increased surface area available for catalytic reactions. However, as the doping concentrations exceeded the optimum levels, the excessive presence of dopants caused light scattering, hindering the effective penetration of light into the suspension. This reduced the overall efficiency of the photocatalytic process, resulting in a decrease in the rate constant value [58].

Therefore, it is crucial to optimize the doping concentrations of La and I in order to achieve the highest photocatalytic activity. So, it is clear from above discussion that optimum doping level of La was up to 2% in conjunction with a simultaneous doping of iodine up to 3%. Beyond this the presence of excessive dopants can lead to light scattering and a subsequent decline in the rate constant, which is confirmed by Table 5.4. The obtained kinetics results from this study are comparable to those reported in Table 5.3.

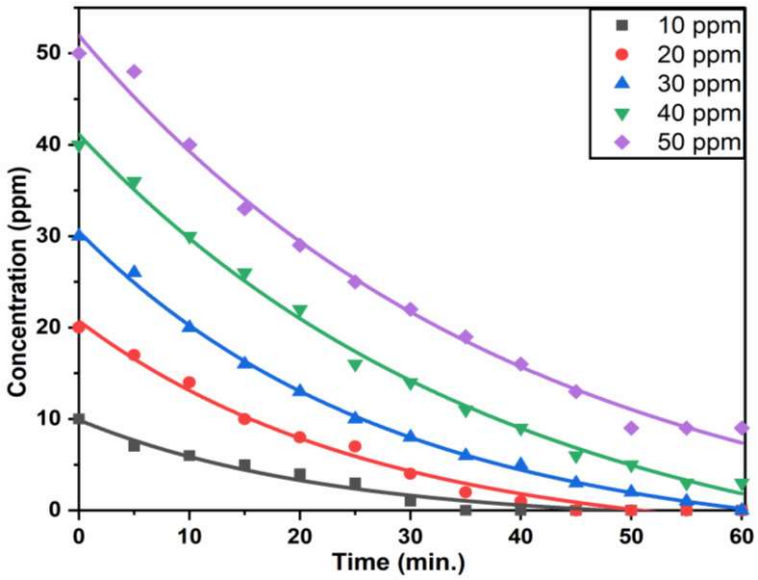

Figure 5.10 Kinetic analysis of MB dye degradation with T8 photocatalyst at catalyst dose of 0.1 g L^{-1}, volume of solution 100 mL and pH 9

Table 5.4 Summary of the degree of fitting (R^2) and reaction rate constants of the undoped and LICT photocatalysts.

	10 ppm		20 ppm		30 ppm		40 ppm		50 ppm	
Cat.	k_p	R^2	k_p	R^2	k_p	R^2	k_p	R^2	k_p	R^2
T0	0.034	0.988	0.033	0.988	0.033	0.972	0.032	0.993	0.030	0.988
T1	0.041	0.985	0.039	0.986	0.037	0.941	0.036	0.964	0.035	0.971
T2	0.042	0.988	0.04	0.983	0.039	0.954	0.037	0.974	0.036	0.976
T3	0.044	0.979	0.041	0.989	0.04	0.961	0.038	0.951	0.037	0.967
T4	0.047	0.981	0.046	0.986	0.044	0.968	0.041	0.955	0.040	0.96
T5	0.051	0.988	0.048	0.987	0.047	0.968	0.045	0.941	0.044	0.967
T6	0.053	0.986	0.050	0.985	0.048	0.99	0.047	0.969	0.046	0.977
T7	0.056	0.988	0.053	0.978	0.051	0.991	0.050	0.969	0.049	0.987
T8	0.064	0.979	0.062	0.984	0.060	0.993	0.058	0.961	0.057	0.982
T9	0.062	0.988	0.060	0.981	0.059	0.983	0.056	0.982	0.055	0.966
T10	0.060	0.975	0.058	0.978	0.057	0.956	0.056	0.975	0.054	0.975
T11	0.058	0.991	0.056	0.972	0.055	0.957	0.053	0.966	0.052	0.974
T12	0.057	0.989	0.054	0.98	0.053	0.969	0.051	0.994	0.050	0.975
T13	0.055	0.99	0.053	0.956	0.052	0.974	0.052	0.986	0.050	0.978
T14	0.051	0.989	0.049	0.982	0.047	0.994	0.046	0.993	0.046	0.961
T15	0.049	0.989	0.046	0.982	0.045	0.994	0.044	0.993	0.043	0.936
T16	0.047	0.989	0.044	0.982	0.042	0.994	0.041	0.993	0.040	0.936
T17	0.045	0.991	0.043	0.978	0.040	0.992	0.039	0.949	0.039	0.969
T18	0.044	0.991	0.042	0.99	0.040	0.989	0.038	0.957	0.037	0.96
T19	0.042	0.981	0.039	0.968	0.037	0.966	0.036	0.975	0.036	0.947
T20	0.040	0.972	0.037	0.978	0.036	0.979	0.034	0.977	0.033	0.983
T21	0.039	0.982	0.035	0.973	0.034	0.963	0.033	0.986	0.033	0.984
T22	0.038	0.974	0.034	0.984	0.032	0.965	0.032	0.966	0.031	0.993
T23	0.037	0.986	0.032	0.996	0.030	0.985	0.029	0.981	0.029	0.973
T24	0.036	0.994	0.031	0.973	0.029	0.996	0.028	0.973	0.029	0.962
T25	0.035	0.997	0.031	0.975	0.028	0.971	0.028	0.981	0.028	0.977

k_p is in min^{-1}

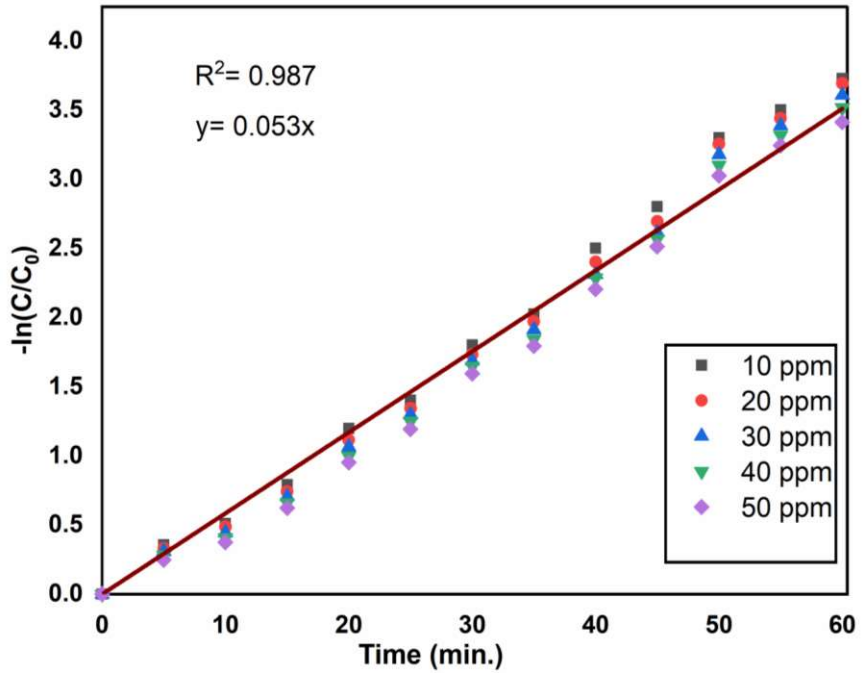

Figure 5.11 Kinetic analysis of the degradation of MB dye by T8 photocatalyst at catalyst dose of 0.1 g L^{-1}, volume of solution 100 mL, -ln(C/Co) vs t data

5.3.6 Reusability and comparative study of the catalysts:

The ability to recycle a photocatalyst is crucial for economics. Therefore, the T8 catalyst was regenerated and reused for MB dye degradation in UV light. The trials were repeated five times in a row, and the findings are depicted in Figure 5.12. After the initial kinetic study, the catalyst was removed with a fresh catalyst and regenerated. The kinetic studied were carried out with a regenerated catalyst, and the percent removal was calculated after 40 min. The photocatalyst's degradation efficiency has dropped after a few experiments. This may be due to systemic effects or the blocking of active sites after the photocatalyst has been cleaned and reused [59]. In our case the loss of efficiency was only 11.67 % after five cycles.

As can be observed in Figure 5.13, FTIR spectra were obtained immediately following the reusability experiments to monitor photocatalyst stability. Even after five successive

degradations, the photocatalyst showed a minor, imperceptible variation in its spectrum. Figure 5.14 displays a comparison of performance in terms of degradation kinetic study among Aeroxide P-25, the best LICT sample, i.e., T8, and the synthesised undoped TiO_2 under UV light. According to the findings, T8 performed best in terms of photocatalytic activity.

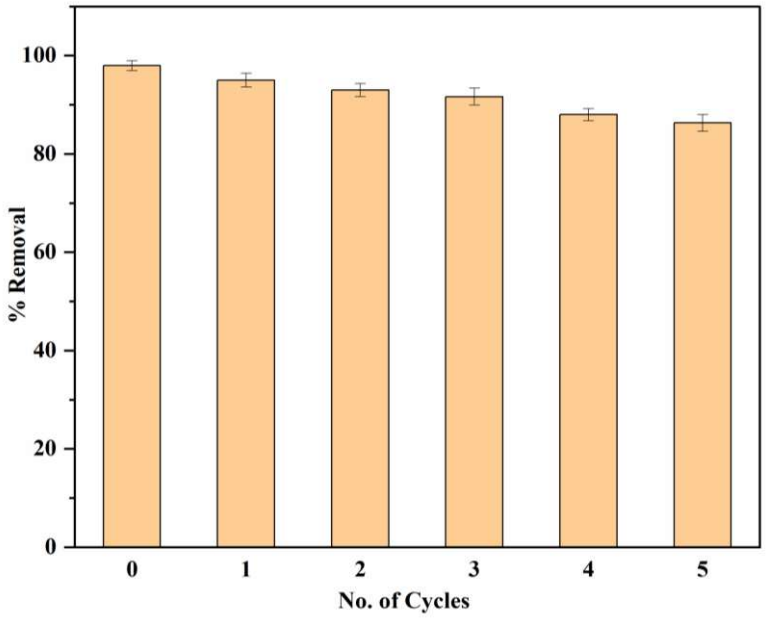

Figure 5.12 The reusability of LICT for the degradation of MB dye at 30 ppm.

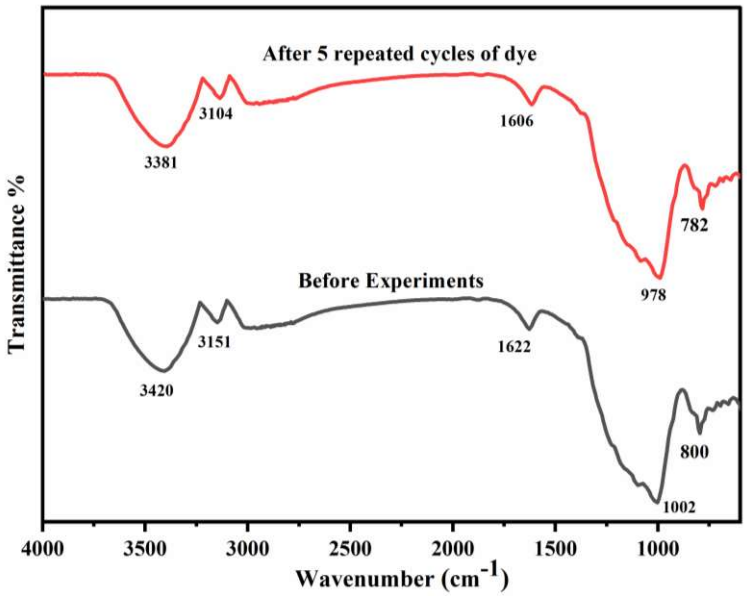

Figure 5.13 FTIR spectra of the regenerated T8 photocatalyst.

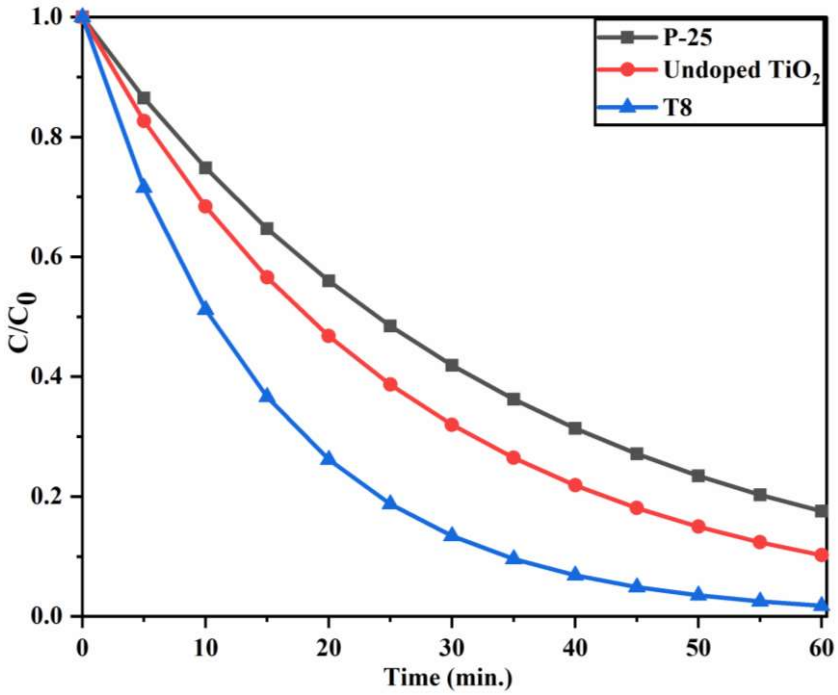

Figure 5.14 Comparison of the best photocatalyst for 30 ppm MB dye degradation using undoped TiO_2, T8, and Aeroxide P-25.

5.3.7 Phytotoxicity analysis:

To assess the phytotoxicity of the treated dye solution (the solution obtained after treatment of 30 ppm MB dye solution with T8 photocatalyst), the germination of *Vigna radiata* seeds was used. Figure 5.15 illustrates the seed germination process for different germination phases for *Vigna radiata* seeds after two days and five days. The results obtained are presented in Table 5.5.

The germination was found to be low in phytotoxicity test in *Vigna radiata* (70%) seeds irrigated with 30 ppm of MB (untreated water), whereas 90% with treated water and 100% with control (distilled water). The germination index was 52.5, 90, 100% respectively. The root and shoot development were significantly higher when seeds were irrigated with the treated water in comparison with untreated. The study revealed that the disparity in the length of roots and shoots of seeds compared to the control group was marginally

lower yet significantly greater than that of the untreated water.

Additionally, the PIN (Phytotoxicity index) of the treated sample was considerably superior to that of the untreated sample. However, the GIN (Germination index) value is more similar to the control seeds. A positive correlation exists between the GIN value and the rate of germination. Based on the analysis of various parameters critical to evaluating seed growth, it can be inferred that the phytotoxicity of treated samples is lower than untreated if used for irrigation.

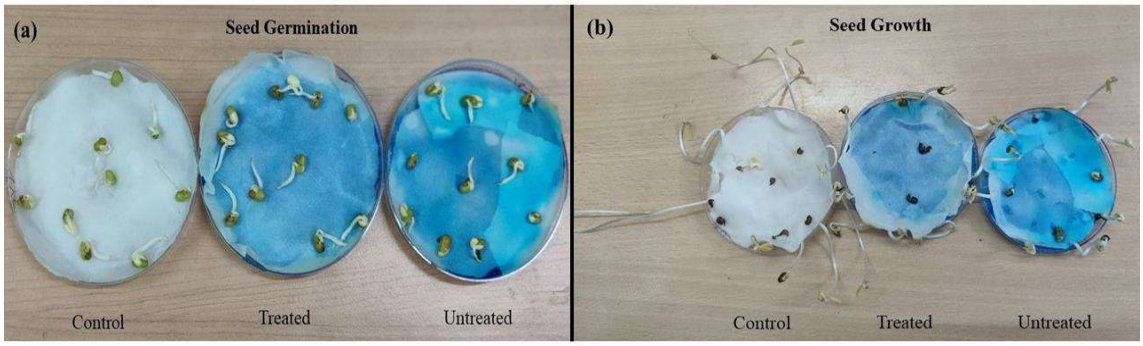

Figure 5.15 (a) Seed germination of control, Treated and untreated sample at t = 2 days (b) Seed growth of control, Treated and untreated sample at t = 5 days

Table 5.5 Toxicity assessment of residual MB solution after photodegradation on Vigna radiata seeds in control, treated and untreated sample.

Sample	Root Length (cm)	Shoot Length (cm)	% RG	% SG	PIN	% GIN
Treated	2 ± 0.14	6 ± 0.26	100	90	0	90
Untreated	1.5 ± 0.16	4 ± 0.19	75	70	25	52.5
Control	2 ± 0.11	16 ± 0.47	100	100	0	100

% RG: % Relative root growth; % SG: % Relative seed germination; PI: Phytotoxicity index; % GIN: % Germination index.

5.4 Conclusion:

The solution-combustion method was used to prepare undoped and LICT nanoparticles successfully. The nanoparticles underwent characterization using XRD, DRS, FTIR, and XPS. The photodegradation of the MB dye was employed to assess the photocatalytic performance of prepared photocatalysts. All the kinetic studies on the photocatalysts show that the T8 photocatalyst has the highest photocatalytic activity. Also, the optimum level of MB degradation, 98%, was achieved by catalyst dose of 0.1 g L^{-1}, pH of 9, an initial concentration of 10 ppm of MB, and 40 min of exposure to UV light. The catalyst T8 was regenerated and used again. The dye was degraded by photocatalyst in UV light, and the results showed that the activity of regenerated T8 photocatalyst diminished with the number of times it was regenerated. The prepared T8 photocatalyst outperformed both bare TiO_2 and Aeroxide P-25 in terms of photocatalytic activity. The evaluation of phytotoxicity demonstrates that the treated MB-bearing water is much less phytotoxic then untreated during germination of *Vigna radiata* seeds.

The germination was found to be low in phytotoxicity test in *Vigna radiata* (70%) seeds irrigated with 30 ppm of MB (untreated water), whereas 90% with treated water and 100% with control (distilled water). The germination index was 52.5, 90, 100% respectively. The root and shoot development were significantly higher when seeds were irrigated with the treated water in comparison with untreated.

References

[1] Z. He *et al.*, "A visible light-driven titanium dioxide photocatalyst co-doped with lanthanum and iodine: An application in the degradation of oxalic acid," *J. Phys. Chem. C*, vol. 112, no. 42, pp. 16431–16437, 2008, doi: 10.1021/jp803291c

[2] L. Li, H. Zhuang, and D. Bu, "Characterization and activity of visible-light-driven TiO_2 photocatalyst codoped with lanthanum and iodine," *Appl. Surf. Sci.*, vol. 257, no. 21, pp. 9221–9225, Aug. 2011, doi: 10.1016/j.apsusc.2011.06.007

[3] M. Baruah, S. L. Ezung, A. Supong, P. C. Bhomick, S. Kumar, and D. Sinha,

"Synthesis, characterization of novel Fe-doped TiO_2 activated carbon nanocomposite towards photocatalytic degradation of Congo red, E. coli, and S. aureus," *Korean J. Chem. Eng.*, vol. 38, no. 6, pp. 1277–1290, 2021, doi: 10.1007/s11814-021-0830-4

[4] H. Shi, T. Zhang, and H. Wang, "Preparation and photocatalytic activity of La^{3+} and Eu^{3+} co-doped TiO_2 nanoparticles: Photo-assisted degradation of methylene blue," *J. Rare Earths*, vol. 29, no. 8, pp. 746–752, 2011, doi: 10.1016/S1002-0721(10)60535-2

[5] C. C. Ho, F. Kang, G. M. Chang, S. J. You, and Y. F. Wang, "Application of recycled lanthanum-doped TiO_2 immobilized on commercial air filter for visible-light photocatalytic degradation of acetone and NO," *Appl. Surf. Sci.*, vol. 465, no. March 2018, pp. 31–40, 2019, doi: 10.1016/j.apsusc.2018.09.136

[6] Z.N. Kayani, S. Rahim, R. Sagheer, S. Riaz, S. Naseem, Assessment of antibacterial and optical features of sol-gel dip coated La doped TiO2 thin films, Mater. Chem. Phys. 250 (2020) 123217. https://doi.org/10.1016/j.matchemphys.2020.123217.

[7] S. Saroj, L. Singh, and S. V. Singh, "Solution-combustion synthesis of anion (iodine) doped TiO_2 nanoparticles for photocatalytic degradation of Direct Blue 199 dye and regeneration of used photocatalyst," *J. Photochem. Photobiol. A Chem.*, vol. 396, no. April, p. 112532, 2020, doi: 10.1016/j.jphotochem.2020.112532

[8] M. Wang, X. Xu, L. Lin, and D. He, "Gd-La codoped TiO_2 nanoparticles as solar photocatalysts," *Prog. Nat. Sci. Mater. Int.*, vol. 25, no. 1, pp. 6–11, 2015, doi: 10.1016/j.pnsc.2015.01.002

[9] X. Chen *et al.*, "Synthesis of visible light responsive iodine-doped mesoporous TiO_2 by using biological renewable lignin as template for degradation of toxic organic pollutants," *Appl. Catal. B Environ.*, vol. 252, no. April, pp. 152–163, 2019, doi: 10.1016/j.apcatb.2019.04.034

[10] I. Arora, H. Chawla, A. Chandra, S. Sagadevan, S. Garg, Advances in the strategies for enhancing the photocatalytic activity of TiO_2: Conversion from UV-light active to visible-light active photocatalyst, Inorg. Chem. Commun. 143 (2022) 109700. https://doi.org/10.1016/j.inoche.2022.109700.

[11] T. Lv, J. Zhao, M. Chen, K. Shen, D. Zhang, J. Zhang, G. Zhang, Q. Liu, Boosted visible-light photodegradation of methylene blue by V and Co co-doped TiO_2, Materials (Basel). 11 (2018). https://doi.org/10.3390/ma11101946.

[12] R. Long, Y. Dai, and B. Huang, "Structural and electronic properties of iodine-doped anatase and rutile TiO_2," *Comput. Mater. Sci.*, vol. 45, no. 2, pp. 223–228, 2009, doi: 10.1016/j.commatsci.2008.09.011

[13] M. Hajizadeh-Oghaz, "Synthesis and characterization of Nb-La co-doped TiO_2 nanoparticles by sol-gel process for dye-sensitized solar cells," *Ceram. Int.*, vol. 45, no. 6, pp. 6994–7000, 2019, doi: 10.1016/j.ceramint.2018.12.200

[14] R. Djellabi *et al.*, "Unravelling the mechanistic role of Ti–O–C bonding bridge at titania/lignocellulosic biomass interface for Cr(VI) photoreduction under visible light," *J. Colloid Interface Sci.*, vol. 553, pp. 409–417, 2019, doi: 10.1016/j.jcis.2019.06.052

[15] A. A. Isari, F. Hayati, B. Kakavandi, M. Rostami, M. Motevassel, and E. Dehghanifard, "N, Cu co-doped TiO_2@functionalized SWCNT photocatalyst coupled with ultrasound and visible-light: An effective sono-photocatalysis process for pharmaceutical wastewaters treatment," *Chem. Eng. J.*, vol. 392, no. November 2019, p. 123685, 2020, doi: 10.1016/j.cej.2019.123685

[16] A. A. Isari, A. Payan, M. Fattahi, S. Jorfi, and B. Kakavandi, "Photocatalytic degradation of rhodamine B and real textile wastewater using Fe-doped TiO_2 anchored on reduced graphene oxide (Fe-TiO_2 /rGO): Characterization and feasibility, mechanism and pathway studies," *Appl. Surf. Sci.*, vol. 462, no. August, pp. 549–564, 2018, doi: 10.1016/j.apsusc.2018.08.133

[17] R. P. Barkul, M. K. Patil, S. M. Patil, V. B. Shevale, and S. D. Delekar, "Sunlight-assisted photocatalytic degradation of textile effluent and Rhodamine B by using iodine doped TiO_2 nanoparticles," *J. Photochem. Photobiol. A Chem.*, vol. 349, pp. 138–147, 2017, doi: 10.1016/j.jphotochem.2017.09.011

[18] C. P. Sibu, S. R. Kumar, P. Mukundan, and K. G. K. Warrier, "Structural modifications and associated properties of lanthanum oxide doped sol-gel nanosized titanium oxide," *Chem. Mater.*, vol. 14, no. 7, pp. 2876–2881, 2002, doi: 10.1021/cm010966p

[19] S. Liu, J. Yu, M. Jaroniec, Tunable photocatalytic selectivity of hollow TiO2 microspheres composed of anatase polyhedra with exposed {001} facets, J. Am. Chem. Soc. 132 (2010) 11914–11916. https://doi.org/10.1021/ja105283s.

[20] R. Asahi, T. Morikawa, H. Irie, T. Ohwaki, Nitrogen-doped titanium dioxide as visible-light-sensitive photocatalyst: Designs, developments, and prospects, Chem. Rev. 114 (2014) 9824–9852. https://doi.org/10.1021/cr5000738.

[21] A. Bashir, F. Bashir, M. Sultan, M. Mubeen, A. Iqbal, and Z. Akhter, "Influence of nickel and lanthanum ions co-doping on photocatalytic properties of TiO_2 for effective degradation of reactive yellow 145 in the visible region," *J. Sol-Gel Sci. Technol.*, vol. 93, no. 2, pp. 438–451, 2020, doi: 10.1007/s10971-019-05162-5

[22] S. Bagwasi, B. Tian, F. Chen, and J. Zhang, "Synthesis, characterization and application of iodine modified titanium dioxide in phototcatalytical reactions under visible light irradiation," *Appl. Surf. Sci.*, vol. 258, no. 8, pp. 3927–3935, 2012, doi: 10.1016/j.apsusc.2011.12.066

[23] R. Anisha and E. K. Kirupa Vasam, "Enhanced photocatalytic degradation of azo dye using rare-earth metal doped TiO_2 under visible light irradiation," *Indian J. Chem. Technol.*, vol. 29, no. 5, pp. 547–553, 2022, doi: 10.56042/ijct.v29i5.62325

[24] W. Reinhardt, Zum frühen Deichbau im niedersächsischen Küstengebiet, Probl. Der Küstenforsch. Im Südlichen Nord. 15 (1984) 29–40.

[25] R. Asahi, T. Morikawa, T. Ohwaki, K. Aoki, Y. Taga, Visible-light photocatalysis in nitrogen-doped titanium oxides, Science (80-.). 293 (2001) 269–271. https://doi.org/10.1126/science.1061051.

[26] L. Li, H. Zhuang, D. Bu, Characterization and activity of visible-light-driven TiO 2 photocatalyst codoped with lanthanum and iodine, Appl. Surf. Sci. 257 (2011) 9221–9225. https://doi.org/10.1016/j.apsusc.2011.06.007.

[27] M. Dorraj, B. T. Goh, N. A. Sairi, P. M. Woi, and W. J. Basirun, “Improved visible-light photocatalytic activity of TiO_2 co-doped with copper and iodine,” *Appl. Surf. Sci.*, vol. 439, pp. 999–1009, 2018, doi: 10.1016/j.apsusc.2017.12.248

[28] B. A. Marinho, R. O. Cristóvão, R. Djellabi, J. M. Loureiro, R. A. R. Boaventura, and V. J. P. Vilar, “Photocatalytic reduction of Cr(VI) over TiO_2-coated cellulose acetate monolithic structures using solar light,” *Appl. Catal. B Environ.*, vol. 203, pp. 18–30, 2017, doi: 10.1016/j.apcatb.2016.09.061

[29] X. F. Lei, C. Chen, X. Li, X. X. Xue, and H. Yang, “Characterization and photocatalytic performance of la and C co-doped anatase TiO_2 for photocatalytic reduction of Cr(VI),” *Sep. Purif. Technol.*, vol. 161, pp. 8–15, 2016, doi: 10.1016/j.seppur.2016.01.030

[30] P. Parthasarathy and S. K. Narayanan, “Effect of Hydrothermal Carbonization Reaction Parameters on,” *Environ. Prog. Sustain. Energy*, vol. 33, no. 3, pp. 676–680, 2014, doi: 10.1002/ep

[31] M. Han *et al.*, “The role of lanthanum in improving the visible-light photocatalytic activity of TiO_2 nanoparticles prepared by hydrothermal method,” *Appl. Phys. A Mater. Sci. Process.*, vol. 126, no. 12, pp. 1–10, 2020, doi: 10.1007/s00339-020-04135-8

[32] Y. Cong, B. Tian, and J. Zhang, “Improving the thermal stability and photocatalytic activity of nanosized titanium dioxide via La^{3+} and N co-doping,” *Appl. Catal. B Environ.*, vol. 101, no. 3–4, pp. 376–381, 2011, doi: 10.1016/j.apcatb.2010.10.006

[33] X. Lan, L. Wang, B. Zhang, B. Tian, and J. Zhang, “Preparation of lanthanum and boron co-doped TiO_2 by modified sol-gel method and study their photocatalytic activity,” *Catal. Today*, vol. 224, pp. 163–170, 2014, doi: 10.1016/j.cattod.2013.10.062

[34] J. Liqiang, S. Xiaojun, X. Baifu, W. Baiqi, C. Weimin, and F. Honggang, “The preparation and characterization of la doped TiO_2 nanoparticles and their photocatalytic activity,” *J. Solid State Chem.*, vol. 177, no. 10, pp. 3375–3382, Oct. 2004, doi: 10.1016/j.jssc.2004.05.064

[35] L. Yu, X. Yang, J. He, Y. He, and D. Wang, “A fluorine free method to synthesize nitrogen and lanthanum co-doped TiO_2 nanocrystals with exposed {0 0 1} facets for enhancing visible-light photocatalytic activity,” *J. Mol. Catal. A Chem.*, vol. 399, pp. 42–47, 2015, doi: 10.1016/j.molcata.2015.01.022

[36] H. Gai *et al.*, “Potassium and iodide codoped mesoporous titanium dioxide for enhancing photocatalytic degradation of phenolic compounds,” *Chem. Phys. Lett.*, vol. 767, no. November 2020, p. 138367, 2021, doi: 10.1016/j.cplett.2021.138367

[37] X. Wang *et al.*, “Activated carbon-based magnetic TiO_2 photocatalyst codoped with iodine and nitrogen for organic pollution degradation,” *Appl. Surf. Sci.*, vol. 390, pp. 190–201, 2016, doi: 10.1016/j.apsusc.2016.08.040

[38] Y. Liu, H. Ran, J. Fan, X. Zhang, J. Mao, and G. Shao, “Fabrication and photovoltaic performance of niobium doped TiO_2 hierarchical microspheres with exposed {001} facets and high specific surface area,” *Appl. Surf. Sci.*, vol. 410, pp. 241–248, 2017, doi: 10.1016/j.apsusc.2017.03.085

[39] R. Saini and P. Kumar, “Green synthesis of TiO_2 nanoparticles using Tinospora cordifolia plant extract & its potential application for photocatalysis and antibacterial activity,” *Inorg. Chem. Commun.*, vol. 156, no. July, p. 111221, 2023, doi: 10.1016/j.inoche.2023.111221

[40] P. Anilkumar, T. Kalaivani, S. Deepak, J. Jasmin, A. F. A. El-rehim, and E. R. Kumar, Journal of *Ceram. Int.*, 2023, doi: 10.1016/j.ceramint.2023.02.061

[41] S. A. Alim, T. S. Rao, S. R. Miditana, and K. V. D. Lakshmi, “Efficient and recyclable visible light-active nickel–phosphorus co-doped TiO_2 nanocatalysts for the abatement of methylene blue dye,” *J. Nanostructure Chem.*, vol. 10, no. 3, pp. 211–226, 2020, doi: 10.1007/s40097-020-00343-z

[42] F. Azeez *et al.*, “The effect of surface charge on photocatalytic degradation of methylene blue dye using chargeable titania nanoparticles,” *Sci. Rep.*, vol. 8, no. 1, pp. 1–9, 2018, doi: 10.1038/s41598-018-25673-5

[43] S. Bibi *et al.*, “Photocatalytic degradation of malachite green and methylene blue over reduced graphene oxide (rGO) based metal oxides (rGO-Fe_3O_4/TiO_2) nanocomposite under UV-visible light irradiation,” *J. Environ. Chem. Eng.*, vol. 9, no. 4, p. 105580, 2021, doi: 10.1016/j.jece.2021.105580

[44] S. Krishnan and A. Shriwastav, “Application of TiO_2 nanoparticles sensitized with natural chlorophyll pigments as catalyst for visible light photocatalytic degradation of methylene blue,” *J. Environ. Chem. Eng.*, vol. 9, no. 1, p. 104699, 2021, doi: 10.1016/j.jece.2020.104699

[45] I. Singh and B. Birajdar, “Synthesis, characterization and photocatalytic activity of mesoporous Na-doped TiO_2 nano-powder prepared via a solvent-controlled non-aqueous sol-gel route,” *RSC Adv.*, vol. 7, no. 85, pp. 54053–54062, 2017, doi: 10.1039/c7ra10108b

[46] E. M. Bayan, T. G. Lupeiko, L. E. Pustovaya, and M. G. Volkova, “Synthesis and photocatalytic properties of Sn-TiO_2 nanomaterials,” *J. Adv. Dielectr.*, vol. 10, no. 1–2, pp. 1–10, 2020, doi: 10.1142/S2010135X20600188

[47] I. Ali and J. O. Kim, “Visible-light-assisted photocatalytic activity of bismuth-TiO_2 nanotube composites for chromium reduction and dye degradation,” *Chemosphere*, vol. 207, pp. 285–292, 2018.
doi: 10.1016/j.chemosphere.2018.05.075.

[48] A. Sikirman and J. Krishnan, “Photocatalytic Degradation of Methylene Blue by Nanosized Visible Light Active Nitrogen and Iron Co-doped Titania: Characterization and Feasibility Investigation,” *J. Environ. Eng.*, vol. 142, no. 9, pp. 1–8, 2016, doi: 10.1061/(asce)ee.1943-7870.0001028

[49] M. Kunnamareddy, R. Rajendran, M. Sivagnanam, R. Rajendran, and B. Diravidamani, “Nickel and sulfur codoped TiO_2 nanoparticles for efficient visible light photocatalytic activity,” *J. Inorg. Organomet. Polym. Mater.*, vol. 31, no. 6, pp. 2615–2626, 2021, doi: 10.1007/s10904-021-01914-5

[50] S. Mishra, N. Chakinala, A. G. Chakinala, and P. K. Surolia, “Photocatalytic degradation of methylene blue using monometallic and bimetallic Bi-Fe doped TiO_2,” *Catal. Commun.*, vol. 171, no. August, p. 106518, 2022, doi: 10.1016/j.catcom.2022.106518

[51] M. Shaban, A. M. Ahmed, N. Shehata, M. A. Betiha, and A. M. Rabie, “Ni-doped and Ni/Cr co-doped TiO_2 nanotubes for enhancement of photocatalytic degradation of methylene blue,” *J. Colloid Interface Sci.*, vol. 555, pp. 31–41, 2019, doi: 10.1016/j.jcis.2019.07.070

[52] J. Su, L. Zhu, P. Geng, and G. Chen, “Self-assembly graphitic carbon nitride quantum dots anchored on TiO_2 nanotube arrays: An efficient heterojunction for pollutants degradation under solar light,” *J. Hazard. Mater.*, vol. 316, pp. 159–168, 2016, doi: 10.1016/j.jhazmat.2016.05.004

[53] S. O.B. Oppong, W. W. Anku, S. K. Shukla, and P. P. Govender, “Lanthanum doped–TiO_2 decorated on graphene oxide nanocomposite: A photocatalyst for enhanced degradation of acid blue 40 under simulated solar light ,” *Adv. Mater. Lett.*, vol. 8, no. 3, pp. 295–302, 2017, doi: 10.5185/amlett.2017.6826

[54] R. Yadav, T. S. Chundawat, P. K. Surolia, and D. Vaya, “Photocatalytic degradation of textile dyes using β-CD-CuO/ZnO nanocomposite,” *J. Phys. Chem. Solids*, vol. 165, no. January, p. 110691, 2022, doi: 10.1016/j.jpcs.2022.110691

[55] Z. Kalaycıoğlu, B. Özuğur Uysal, Ö. Pekcan, and F. B. Erim, “Efficient Photocatalytic Degradation of Methylene Blue Dye from Aqueous Solution with Cerium Oxide Nanoparticles and Graphene Oxide-Doped Polyacrylamide,” *ACS Omega*, vol. 8, no. 14, pp. 13004–13015, 2023, doi: 10.1021/acsomega.3c00198

[56] Z. Shi, X. Zhang, and S. Yao, “Preparation and photocatalytic activity of TiO_2 nanoparticles co-doped with Fe and la,” *Particuology*, vol. 9, no. 3, pp. 260–264, 2011, doi: 10.1016/j.partic.2010.05.017

[57] J. Li, Y. Zeng, Y. Fang, N. Chen, G. Du, and A. Zhang, “Synthesis of (La + Nb) co-doped TiO_2 rutile nanoparticles and dielectric properties of their derived ceramics composed of submicron-sized grains,” *Ceram. Int.*, vol. 47, no. 7, pp. 8859–8867, 2021, doi: 10.1016/j.ceramint.2020.12.007

[58] A. Hernández-Gordillo and V. R. González, “Silver nanoparticles loaded on Cu-doped TiO_2 for the effective reduction of nitro-aromatic contaminants,” *Chem. Eng. J.*, vol. 261, pp. 53–59, 2015, doi: 10.1016/j.cej.2014.05.148

[59] A. Hassani, M. Faraji, and P. Eghbali, “Facile fabrication of mpg-C_3N_4/Ag/ZnO nanowires/Zn photocatalyst plates for photodegradation of dye pollutant,” *J. Photochem. Photobiol. A Chem.*, vol. 400, no. May, p. 112665, 2020, doi: 10.1016/j.jphotochem.2020.112665